*Real-Time Imaging* **8**, 175–188 (2002)
doi:10.1006/rtim.2002.0284, available online at http://www.idealibrary.com on IDEAL®

# *Multiphoton Imaging of Neurons in Living Tissue: Acquisition and Analysis of Time-Lapse Morphological Data*

Multiphoton laser scanning microscopy offers improved axial resolution over confocal microscopy for three-dimensional (3D) imaging of fluorescently labeled cells. It also greatly reduces phototoxicity and photobleaching outside the plane of focus when collecting 3D series of optical sections in living tissue. This permits images to be collected at shorter intervals with less harm to the specimen. To facilitate the transition from confocal to two-photon *in vivo* imaging, we have compared some of the most commonly used fluorescent vital dyes for their applicability to confocal and two-photon laser scanning microscopy. We find that many of the dyes commonly used for morphological imaging can be used for two-photon excitation microscopy. However, the optimal wavelengths for two-photon excitation cannot always be deduced from the one-photon fluorescence spectra of the fluorophores. As improvements in imaging technology are beginning to make near-real-time *in vivo* fluorescence imaging more feasible, flexible software that can perform temporal as well as spatial analyses of anatomical data becomes increasingly important. Here we demonstrate how we have used Object–Image, an extension of the popular public-domain NIH Image software, together with a set of custom macros for time-lapse morphometric analysis, to analyze neuronal branch growth and complexity in three dimensions over time.



**Edward S. Ruthazer and Hollis T. Cline**

*Cold Spring Harbor Laboratory*
*Cold Spring Harbor*
*NY 11724, USA*
*E-mail: ruthazer@cshl.org, cline@cshl.org*

## Introduction

Neurons exhibit a diverse range of morphologies that reflect their specific functions in the nervous system. During development, neurons can undergo such dramatic changes in their shapes that it may be difficult to recognize that the immature and adult morphologies belong to the very same cell. In addition, short interval time-lapse imaging studies have shown that developing neurons both add and retract many processes over the course of just a few minutes [1]. Images captured at long intervals consequently can fail to represent the high rate of dynamic rearrangements of the branches of axons and dendrites. Thus, an accurate understanding of the development of neuronal morphology can come only from following the structural changes of individually labeled cells over time both at brief intervals and over extended periods.

1077-2014/02/ $35.00

The fundamental challenge in morphological time-lapse imaging is to capture multiple images while introducing minimal damage to the specimen, one major source of which is phototoxicity resulting from the very act of imaging itself. This must be balanced with the need for sufficient detail and accuracy to be confident that any changes detected between images captured at different times are not an artifact of the imaging method. In our experiments imaging the development of neurons in the retinotectal system of living *Xenopus laevis* tadpoles, an additional goal is that conditions be as physiologically normal as possible [2]. Thus, animals are usually returned to their tanks between images, making it difficult to position animals in the exact same orientation at different imaging time points. To reduce the potential artifact arising from variability in specimen orientation, as well as for greater accuracy overall, we currently perform our image acquisition and analysis in three dimensions.

## Methods

### *In vivo single-cell fluorescent labeling*

The labeling methods used in this paper are described in detail in [2] for iontophoresis of lipophilic dye and dextrans, and in [3] for single-cell electroporation of DNA. In brief, 1.5 mm diameter glass micropipettes pulled to a fine tip ($<1\,\mu m$) were filled with a solution of lipophilic dye (Molecular Probes, 0.02% in ethanol), 10K molecular weight fluorescent dextrans (Molecular Probes, 5% w/v in water) or purified bacterial plasmid DNA (Clontech, ~1 μg/μL in water). For dyes, 3–5 pulses of duration 10–100 ms and of 1–10 nA positive current and for DNA negative current pulses with an exponential decay ($\tau = 70$ ms) [3] were applied through the pipette after positioning its tip at a location adjacent to the cell targeted for labeling. For all labeling and imaging procedures, tadpoles were anesthetized in a 0.01% solution of MS-222 dissolved in 10% Steinberg's solution.

### *In vivo confocal and two-photon imaging*

Anesthetized tadpoles were placed in a sylgard mounting chamber on the stage of either a confocal or two-photon laser scanning microscope. The confocal microscope is a Nikon Optiphot with NORAN OZ laser scanning confocal attachment and krypton–argon laser. Confocal *z*-series were collected in 2 μm steps using a 10 μm confocal slit and either a Nikon 40× air ($NA = 0.85$) or 40× oil ($NA = 1.3$) objective. The two-photon microscope is a modified FLUOVIEW 300/ Olympus BX51 microscope [4] with Tsunami tunable femtosecond pulse mode-locked Ti: sapphire laser, pumped by a Millenia V solid-state optical diode laser (Spectra Physics). External photomultiplier tubes (Hamamatsu) with either BG39 or HQ607/45 filters (Chroma) were used to detect emitted light. Modifications were designed primarily by Dr Karel Svoboda (Cold Spring Harbor Laboratory). Images were collected at 1.5 μm intervals using an IR 40× water immersion (Olympus, $NA = 0.8$) objective lens. We do not oversample intensively in the z-axis to reduce photodamage to the specimens.

## Results

### *Visible progress through microscopic advances*

Early experiments used brief flashes of excitation light and high-sensitivity video cameras to capture a fluorescence image of a labeled cell, often limiting imaging to a single focal plane in the sample to reduce photobleaching and damage [5]. The laser scanning confocal microscope offers a considerable improvement in the *z*-axis resolution and signal-to-noise ratio by using a pinhole or slit aperture to eliminate out-of-focus emission light, permitting accurate three-dimensional (3D) *z*-series to be captured [6,7]. In addition, since illumination is achieved by raster scanning a single beam of excitation light across the *x* and *y* dimensions of the sample, it becomes practical to use an individual or small number of extremely sensitive, though costly, photomultiplier tubes (PMT) to detect the emitted fluorescence.

Despite these improvements in resolution and sensitivity, confocal microscopy still provides only a modest reduction in phototoxicity for imaging living tissue. Optical scattering, particularly severe in living tissue, reduces the ability both to excite and to detect emitted photons from within the plane of focus. Since scattered emission light is blocked by the confocal aperture, either a larger aperture with inferior *z*-axis resolution or more intense excitation light, ultimately increasing photodamage, must be used to compensate for lost signal. In addition, scattering makes imaging of fluorescent structures embedded more than a few hundred microns deep in living tissue simply unfeasible [8].

Another critical cause of phototoxic damage when imaging the 3D structure of living cells by confocal microscopy comes from excessive exposure to excitation light outside the plane of focus. In the cone of unfocused excitation light directly above and below the focal plane, the intensity of the beam of excitation light decreases as a direct consequence of its broadening. However, this broadening of the scanning beam effectively lengthens the exposure time to the scanning beam at all out-of-focus points in the sample. Consequently, the cumulative amount of exposure to harmful excitation light is as great outside as within the plane of focus. The resulting out-of-focus emission light has little impact on image quality as it is blocked from reaching the PMT by the confocal aperture, but by then the damage to the tissue is already done.

*Deus ex Machina: multiphoton excitation laser scanning microscopy*

Multiphoton excitation laser scanning microscopy (MPLSM) elegantly solves both these problems by limiting excitation of the fluorophore to the plane of focus [9, 10]. Multiphoton excitation occurs as a result of rare, coincident absorption of two or more low-energy photons by a fluorophore molecule. Since there is a nonlinear dependence of multiphoton excitation on illumination intensity, illumination through the microscope objective effectively restricts multiphoton excitation to the plane where the excitation beam is focused to an intense spot of high photon density. Outside the focal plane, the long-wavelength excitation light, which is not readily absorbed by tissue in the form of one-photon excitation, is mostly inert. An added advantage of the longer wavelength light used for multiphoton imaging is a reduction in scattering and absorption, which can be severe in living tissue, permitting crisp imaging at greater depths than could otherwise be achieved using confocal microscopy (Figure 1) [11–13].

In contrast to confocal microscopes, which achieve depth resolution by discarding out-of-focus light using the pinhole aperture, multiphoton microscopy assures that nearly all fluorescence emission light originates from the targeted site in the sample. This means, in principle, that all the emitted light of the appropriate wavelength can be collected without descanning through a pinhole and used for reconstruction of the image, greatly augmenting the potential sensitivity of the microscope and reducing photobleaching and photodynamic damage (Figure 2) [14]. For example, a high numerical aperture (NA) condenser projecting to a separate set of PMTs can be used efficiently to collect transmitted fluorescence light beneath the sample that would otherwise be entirely lost in a confocal system [15].

Two predicted shortcomings of multiphoton microscopy compared to one-photon confocal microscopy are reduced spatial resolution and inferior fluorophore selectivity. Under optimal conditions, the longer wavelengths used for two-photon microscopy theoretically should only provide about half the lateral and axial precision achievable with the shorter wavelengths used for one-photon excitation. However, we have found that under the conditions of our imaging experiments, both methods produce comparable images, in particular, near the tissue surface where confocal performance is less severely impeded by optical scattering (Figure 3).

Another limitation of multiphoton microscopy is the broad excitation spectra of many molecules [16]. Since many fluorophores with non-overlapping one-photon absorption spectra exhibit considerable overlap in their two-photon cross sections, we find that it is often more difficult to exclusively excite one fluorophore in double-labeled material by two-photon excitation than by one-photon excitation. The opportunity that exists on the confocal microscope to select both the excitation and emission wavelengths of the fluorophore of interest naturally offers greater discrimination when imaging double-labeled samples. Moreover, tissue autofluorescence in biological samples, which is strongly excited by blue light and thus can be largely avoided in one-photon microscopy by using red fluorophores, is in some cases more problematic with two-photon excitation.

In the majority of cases, however, different fluorophores can be adequately distinguished by their emission wavelengths. Indeed, by using multiple PMTs, each with filter sets optimized for different emission ranges, it is possible to discriminate between several different fluorophores imaged simultaneously using the same wavelength of excitation light. This means that chromatic aberration of the optics has no effect on the spatial alignment of images collected using different color fluorophores. In contrast, confocal microscopes typically require elaborate calibration and alignment of each channel in three dimensions for accurate analysis of colocalization. Thus, the development of fluorophores with large two-photon cross sections and well-separated emission spectra will tremendously facilitate the accurate analysis of double-labeled samples [17].

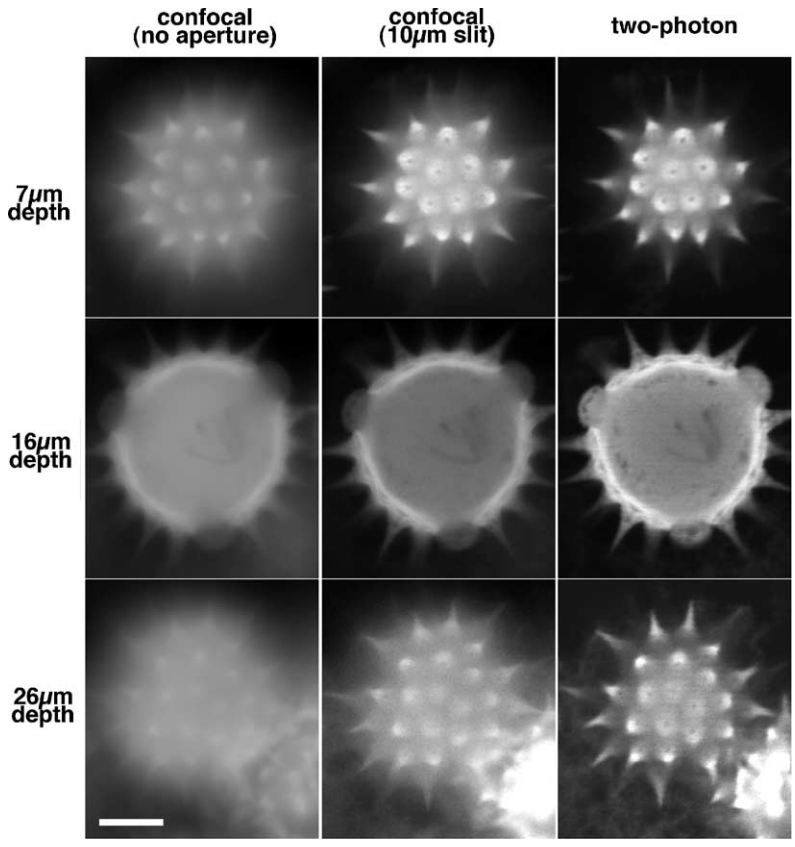


**Figure 1.** Pollen grain - Fluorescent pollen grain was imaged at three depths below its surface (7, 16, and 26 μm) to demonstrate differences between confocal and two-photon laser scanning microscopy. The first column, shows the images captured on a Noran OZ confocal microscope when no confocal aperture is used to exclude out-of-focus light. In the second column, a 10 μm confocal slit is applied. The third column was captured on an Olympus FV300 confocal microscope that has been modified for two-photon excitation. No confocal aperture was used for two-photon imaging. For confocal microscopy, the aperture improves image quality in both superficial and deep optical planes by reducing the contribution of scattered light. Two-photon imaging improves image sharpness over confocal imaging for deep optical sections by reducing scattering of excitation light and by eliminating fluorescence excitation outside the plane of focus. A Nikon 40 × air ($NA = 0.85$) lens was used for the first two columns and an Olympus 40 × water-immersion ($NA = 0.8$) lens was used for the two-photon images. Scale bar = 10 μm.

A more serious drawback of multiphoton microscopy at present is the high cost of mode-locked lasers that deliver 0.1–1 ps pulses at around 100 MHz. These high repetition rate, ultrashort pulse lasers are critical for non-destructive delivery of the high photon densities required for MPLSM. Of the currently available mode-locked lasers, Ti: sapphire lasers offer the most useful spectral range (700–1000 nm) for imaging traditional fluorophores, but rely on expensive argon-ion or Nd: YVO4 diode pump lasers. As the market for these lasers expands, new technological developments may drive down prices and deliver enhanced features. For example, electronically tunable lasers are now available as an alternative to the manually tunable lasers in common use, making more practical the possibility of enhanced fluorophore selectivity in double-labeled samples by alternately stimulating at different wavelengths using an automated process.

*Two-photon imaging using vital dyes*

Vital dyes are biologically inert fluorescent tracers that make it possible to label and image an individual cell among the thousands of other cells that surround it in living tissue. They can be classified into three groups: lipophilic dyes that incorporate into cell membranes, cytosolic dyes of which the fluorescent dye-conjugated dextrans are most prevalent, and fluorescent proteins such as green fluorescent protein (GFP). There has been a proliferation of vital dyes in recent years, particularly

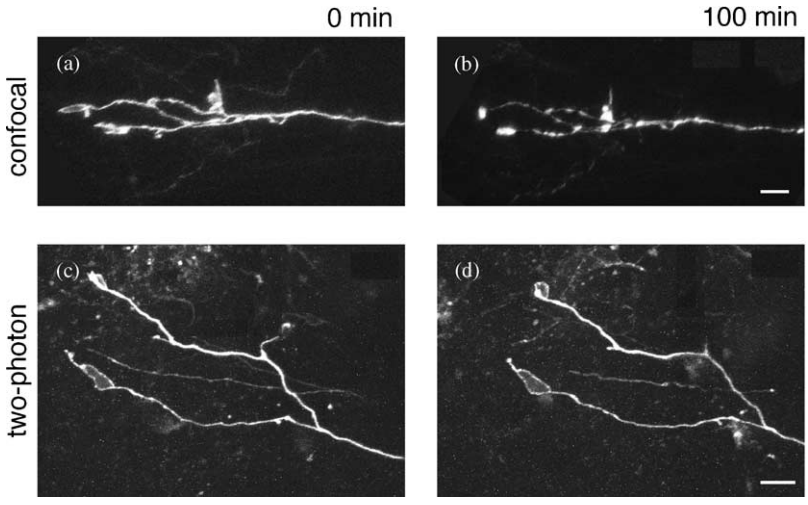


**Figure 2.** Comparison of phototoxicity from confocal microscopy and MPLSM. FITC-dextran labeled retinal ganglion cell axons in the optic tectum were imaged at 10 min intervals for 100 min using confocal or two-photon microscopy. The axon imaged on the confocal microscope gradually develops "blebs" characteristic of photodynamic damage, while the axon imaged on the two-photon microscope maintains its original morphology. (a) Confocal *z*-series projection at time 0 min. (b) Confocal projection at 100 min time point. (c) Two-photon projection at 0 min. (d) Two-photon projection at 100 min timepoint. Scale bar = 10 μm.

among the fluorescently conjugated dextrans, offering a spectral range from ultraviolet (U.V.) to infrared. In this section, we compare several vital dyes that we have tested for *in vivo* imaging with a special focus on their two-photon excitation properties (Table 1).

*Lipophilic dyes*. Lipophilic dyes, which include the carbocyanine dyes (DiI, DiO and DiD) and styryl dyes (DiA, ANEPPS, and FM dyes), are inserted into the plasma membrane of cells where they can diffuse laterally as well as enter the intracellular vesicular pool and be transported actively [18]. When applied iontophoretically to a neuronal cell soma, the dye can be observed diffusing into dendritic processes in seconds and they are fully labeled after a few hours, depending on the size of the dendritic arbor. Anterograde labeling of axons from the cell body is typically complete within 24 h [2]. It is not unusual for axon terminals and growth cones to be more brightly labeled than the intervening stretch of axon between the injection site and terminal, suggesting that active transport and insertion of dye-bearing vesicles to the active growth cone may

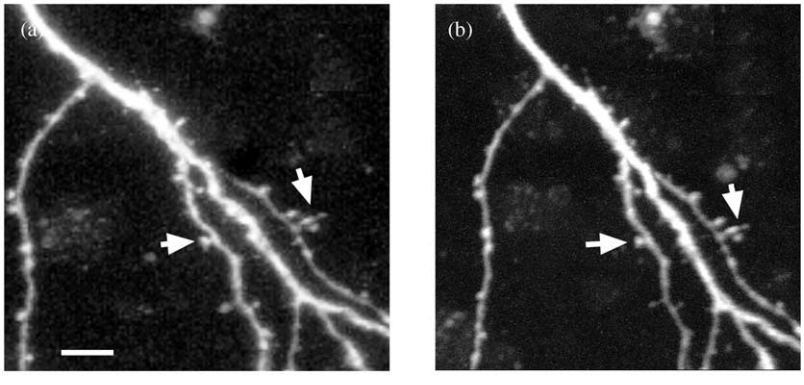


**Figure 3.** Comparable planar resolution in confocal and two-photon images Dendrites and spines (arrow) of a GFP-expressing hippocampal pyramidal cell in an organotypic slice culture imaged by (a) confocal microscopy, using a 40× oil objective ($NA = 1.3$) at 488 nm excitation and (b) MPLSM using a 40× water objective ($NA = 0.8$) at 910 nm excitation. Fine processes like dendritic spines are clearly detected by both methods. Scale bar = 5 μm.

**Table 1.** Comparison of vital dyes for one-photon and two-photon fluorescence imaging of neurons. *Emission intensities were measured in 10 nm steps between 830 and 920 nm at 100 mW laser intensity. Brightness was rated subjectively based on visibility of fine processes in labeled cells. One-photon spectral values are from the manufacturer

| Fluorophore | One-photon excitation max (nm) | Two-photon excitation max (nm)* | Emission (max) | Brightness by one-photon fluorescence excitation | Brightness by two-photon excitation |
|---|---|---|---|---|---|
| DiA | 456 | 880 | 590 | + + | + + + |
| DiD | 644 | 830 | 665 | + + + | – |
| DiI | 549 | 900 | 565 | + + + | – |
| DiO | 484 | 880 | 501 | + + | + + |
| Di-8-ANEPPS | 467 | 880 | 631 | + | + |
| Alexa 488-dextran | 495 | 830 | 519 | + + | + + |
| Alexa 594-dextran | 590 | 840 | 617 | + | + + + |
| FITC-dextran (fluoro-emerald) | 494 | 830 | 521 | + + + | + + |
| Texas Red-dextran | 595 | 880 | 516 | + + | + + |
| TRITC-dextran (fluoro-ruby) | 555 | 850 | 580 | + + | + + + |
| EGFP | 488 | 910 | 507 | + + + | + + + |
| DsRED | 558 | 920 | 583 | + + + | + + + |

contribute to anterograde labeling. Retrograde labeling from terminals also occurs, but can require several days. In stark contrast to the uninterrupted appearance of dye labeling in somatic and axonal fills, retrograde labeling results in a granular distribution of dye in the labeled cell soma, presumably reflecting labeling of the endosomal lipid pool.

Since they passively diffuse into cell membranes, the lipophilic dyes can be applied by simple pressure injection of a solution made up in ethanol or DMSO, or even by direct application of a solid crystal of the dye. We find, however, that for single-cell labeling iontophoretic application of a 0.02–0.2% dye solution in ethanol through a glass micropipette has the highest success rate. For confocal imaging of cells in the retinotectal circuit, DiI and DiD from Molecular Probes both work very well in our hands. Others have also reported bright labeling with DiO [19]. Since DiD is efficiently excited with relatively long-wavelength red light, it is particularly useful for labeling cells more deeply embedded in tissue where scattering can be problematic. It also appears to be less prone to phototoxicity than the other lipophilic dyes. Unfortunately, neither DiI nor DiD appears to be suitable for two-photon imaging, as DiI is only weakly fluorescent by two-photon excitation [16] and DiD excitation is probably too long in wavelength to be excited with the Ti: sapphire laser. We have found that single cells labeled with DiO or the styryl dyes, DiA and to a lesser degree Di-8-ANEPPS, are brightly fluorescent by two-photon excitation around 880 nm (Figure 4(a)). Denk *et al.* have used Di-4-ANEPPS excited at 860 nm to visualize neural tissue [13]. Others have reported using two-photon microscopy to image synaptic vesicle trafficking with the styryl dye FM1-43 [20].

*Fluorescent dextrans.* Dextrans are biologically inert, water-soluble polysaccharides to which a variety of fluorochromes have been conjugated. They can be injected directly into cell somata for lineage or morphology studies, but are also taken up spontaneously when delivered by pressure or iontophoresis just outside cell somata [21]. Dextrans appear to be transported at least as well anterogradely as they are retrogradely making them especially useful for labeling of axons. We regularly use 3000 or 10,000 molecular weight dextrans conjugated to xanthene dyes (FITC, TRITC, Texas red), to Alexa dyes, or to BAPTA analog calcium indicators like Calcium Green, purchased from Molecular Probes. We introduce the fluorescent dextrans either by extracellular iontophoresis or by including them in a patch pipette for electrophysiology [2]. All the dextran conjugates we have tried work well for *in vivo* imaging on both the confocal and two-photon microscopes (Figure 4(b)–(d)). Their quality of labeling is more stable over several days than that of the lipophilic dyes, though the FITC-conjugated dextran does occasionally appear to damage axons when imaged at short ($<2$ h) intervals on the confocal microscope (Figure 2(a) and (b)). The Alexa-conjugated dextrans

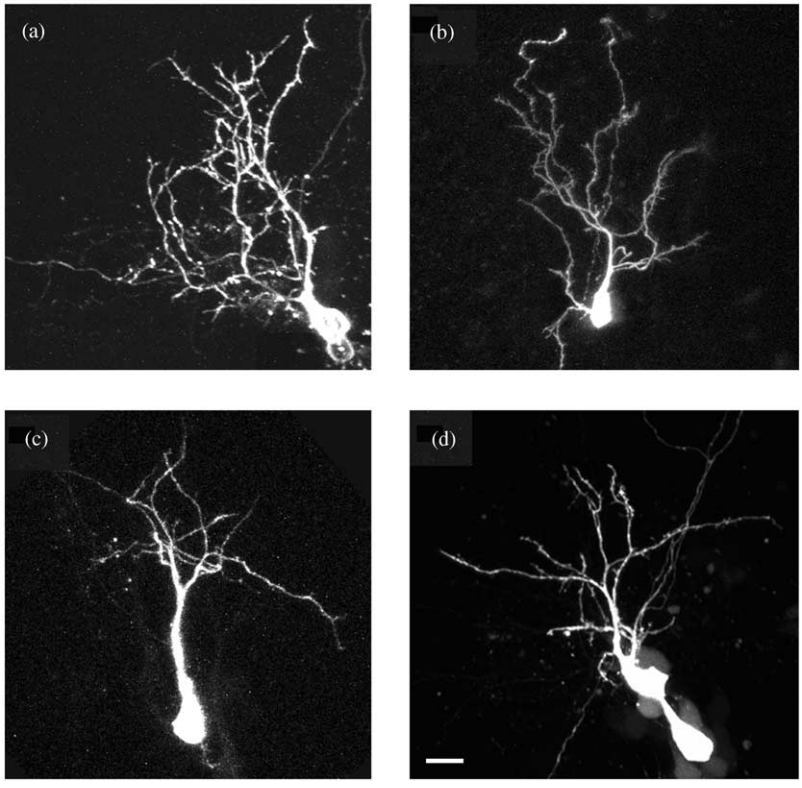


**Figure 4.** Many conventional fluorescent dyes can be used for MPLSM: (a) DiA, (b) FITC-dextran, (c) Texas Red-dextran, and (d) Alexa 594-dextran labeled neurons imaged by two-photon excitation laser scanning microscopy. Scale bar = 10 μm for A, C and D, 15 m for B.

are reputed to be less susceptible to photobleaching and toxicity than their xanthene counterparts. Alexa 594, which is only moderately bright by one-photon microscopy, has an unpredicted two-photon excitation peak around 840 nm that gives a brilliant red emission. This makes it particularly useful for multiple label imaging, since most other fluorophores that excite optimally around 840 nm typically produce fluorescence emission in the green range.

*Green fluorescent protein and its variants*

GFP is a naturally occurring fluorophore that is isolated from the bioluminescent jellyfish *Aequorea victoria* [22]. Since the introduction of the gene encoding GFP into cells of other species results in the expression of active fluorescent protein, persistent fluorescent labeling of individual or small groups of cells transfected with DNA encoding GFP is possible. Individual neurons can be made to express an exogenous GFP gene by many approaches, including viral vectors [23], lipofection [24], biolistics [25], and electroporation [3]. Moreover, by creating transgenic animals in which the gene encoding GFP or GFP fusion proteins is integrated into the genome, cell morphology as well as gene expression and protein targeting can be studied *in situ* with minimally invasive imaging procedures [26]. Since its initial description, numerous variants of GFP, optimized for brightness at a range of different wavelengths, ionic sensitivities, stability, temperature and species-specific codon usage have been created through rational tinkering with the wildtype sequence [22]. Other independent fluorescent proteins like the red fluorescent protein isolated from *Discosoma* coral (dsRed) also have been identified, cloned and modified for specific uses [27].

For morphological studies, transfection with GFP has several important advantages over the labeling methods described above. In contrast to direct injection of fluorescent molecules, GFP expression is a cumulative and regenerative process; cells increase in brightness over time as highly stable GFP molecules accumulate, and can, as a result, recover from photobleaching. The

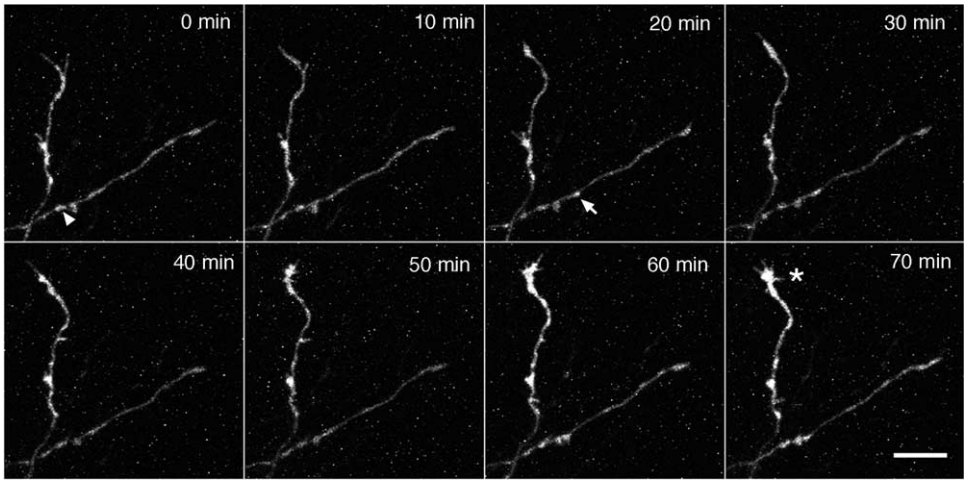


**Figure 5.** Time-lapse imaging of VAMP-GFP in retinotectal axons. Retinal ganglion cells were lipofected with plasmid encoding a fusion of GFP and the rat synaptic vesicle protein VAMP2. The axon terminal was time-lapse imaged by MPLSM at 10 min intervals, revealing stable (arrowhead) and transient (arrow) VAMP-GFP clusters. The axons remain healthy throughout the imaging period, as demonstrated by the active extension of filopodia and lamellipodia by the axonal growth cone (asterisk). Scale bar = 10 μm.

structure of the GFP molecule is a hollow cylinder of 11 rigid $\beta$-sheets surrounding an $\alpha$-helix bearing the chromophore domain [22]. As a result of this rigid shell that partially isolates the fluorophore from the environment, photodynamic damage and bleaching are greatly reduced for GFP compared to most other fluorophores. This combination of high fluorophore concentration and low phototoxicity makes fluorescent proteins like GFP and dsRED ideal for most *in vivo* time-lapse imaging applications. These properties of GFP and dsRED, in conjunction with the benefits of MPLSM, offer an unprecedented opportunity for safe, near-real-time fluorescence imaging of neurons in living tissue. We currently use single-cell electroporation of EGFP, a red-shifted variant of wildtype GFP, for the majority of our single tectal cell time-lapse imaging experiments [3].

One of the most promising uses of the GFP variants is in the construction of fusion proteins in which a gene of interest is modified to include GFP sequence. GFP fluorescence can then be used to monitor the translation and functional trafficking of the protein to which it is fused. In neurons, this approach has been used to demonstrate movement of synaptic vesicle proteins [28] (Figure 5) and translocation of glutamate receptors to synapses [29]. In addition, GFP-based second messenger indicators have been engineered by taking advantage of fluorescence resonance energy transfer (FRET) between two different colored variants of GFP linked by second messenger-responsive peptide domains. For example, the calcium reporter proteins known as "cameleons" are fusions of the calmodulin-binding domain of myosin-light-chain kinase and calmodulin to either GFP/Blue Fluorescent Protein, Cyan Fluorescent Protein/Yellow Fluorescent Protein, or GFP/dsRED pairs [30].

The main concerns over using GFP as a fluorescent tracer stem from the fact that most methods for introducing foreign genes into cells do not permit fine control of protein expression levels. There is little evidence that overexpression of free GFP has any detrimental effects on the cell, but it seems likely that overexpression of GFP-tagged signaling molecules or structural proteins may have unwanted consequences on cellular physiology. Vectors that offer tight control of gene transcription or protein translation levels and timing will be essential for unlocking the full power of GFP as a functional label.

### *Morphometric analysis with public-domain software*

Information from high-resolution imaging data is most valuable when expressed as quantitative measures of spatial and temporal features of neuronal structures. Several laboratories have reported the design of customized systems for computer-assisted neuron reconstruction and analysis [31–34]. There also exist a number of powerful and versatile professional morpho-

logical reconstruction software packages that can cost many thousands of dollars. In most cases, however, a very basic but flexible system will suffice for analysis of experimental data from imaging experiments. For example, our quantitative analyses of *Xenopus* retinal ganglion cell axon and optic tectal cell dendrite development primarily involve just three kinds of measurements:

1. the total 3D axonal or dendritic arbor lengths and growth rates,
2. the rates and locations of branch additions and retractions,
3. local changes in branch density or complexity (e.g. Sholl analysis).

We have found that our analysis requirements are met by the public–domain freeware program Object–Image (downloadable at: http://simon.bio.uva.nl/object-image.html) when combined with a few simple custom analysis macros. Object–Image is Norbert Vischer's extension of NIH Image, the popular image analysis program for the Macintosh platform created by Wayne Rasband at the Research Service Branch of the National Institutes of Health [35]. In Object–Image, a 3D, non-destructive overlay can be drawn manually upon the *z*-series stacks captured by the confocal or two-photon microscopes. Additional detailed information about the images can be accessed and manipulated for further analysis with an easy to use, Pascal-like macro language. Furthermore, using this macro language to create a user interface, it is possible to attach user-generated details, such as branch lifetimes or segment thickness, to each point or segment in the overlay by the use of a "mini-spreadsheet" feature. Thus, with a bare minimum of programming, the Object–Image can be used as a basic but highly versatile 3D neuronal reconstruction system that offers as an additional benefit the extensive image processing capabilities of NIH Image.

This section outlines how we have used the features of Object–Image to perform morphometric analyses that would otherwise require costly professional software packages or extensive custom programming. The macros described herein are available on a remote website as supplementary information (http://www.cshl.edu/labs/cline/morphometry.html). This system has been used in our laboratory for neuron tracing and analysis in several biological experiments that have been published as preliminary reports [36–38].

*Importing image files*. The 8-bit TIFF stack is the standard format for saving microscope *z*-series images for analysis with Object–Image. Original image files of nearly any format can be converted into TIFF stacks using simple programs written in the Object–Image macro language if the user is familiar with the organization of the original file formats. Object–Image lacks sophisticated commands to manage text or other non-graphical information in files. However, by treating the bytes that make up text files or file headers as pixels in an image, it is possible to apply the powerful image manipulation commands of Object–Image to handling non-graphical data. Though quite flexible and high level, macros are considerably slower to execute than compiled code written in lower-level programming languages. It, therefore, may be impractical to use the macro language to decode compressed images or to reassemble highly fragmented images.

Our two-photon microscope is a custom-modified FLUOVIEW FV300 confocal microscope. The Fluoview software saves images in Olympus multi-TIFF format, which obeys most conventions for standard TIFF files but adds additional information about the image look-up table in the header. Since Object–Image can only process 8-bit stacks, and multi-TIFF files have 12 bits of gray-scale resolution per pixel, our conversion macro to open multi-TIFF files also rescales the 12-bit images into the standard 8-bit TIFF format to make it compatible with the software. Our confocal stacks, collected on a NORAN Instruments OZ confocal microscope controlled by a Silicon Graphics Indy computer, are stored as SGI IRIS Movie Format files, which are easily converted in Object–Image to 8-bit TIFF format without requiring significant modifications.

*3D overlay tracing*. The most time-consuming phase of our data analysis is the step of manually tracing the dendritic or axonal processes of a labeled cell. At present, we use the non-destructive, 3D overlay feature of Object–Image to do point-and-click tracing of neuronal processes directly onto the captured *z*-series stacks, entering each individual branch as a separate segmented line. The program records the 3D Cartesian coordinates of each endpoint of the segments that make up the drawing, which then can be used to calculate total branch lengths, branch density and to perform further analyses (Figure 6).

In this respect our data structure differs slightly from that used in most other reconstruction software [31–34]. Since our primary interest is the dynamic addition and retraction of individual branches over time, we have

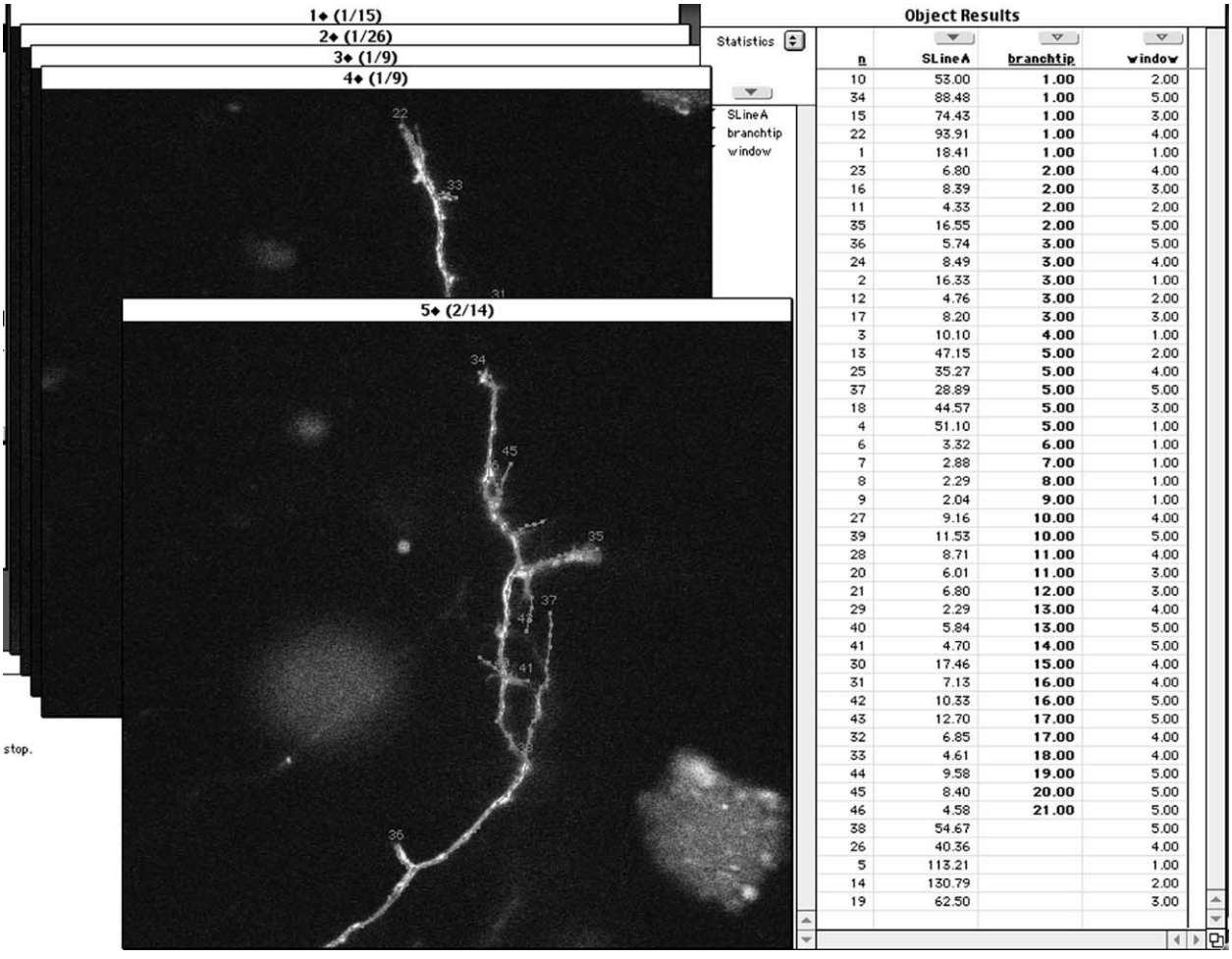


**Figure 6.** Use of the non-destructive overlay in Object–Image to reconstruct axonal arbors. Screenshot showing a set of five *z*-series stacks, images of the same axon imaged at five different time points, on which each individual branch tip has been traced by hand and assigned a reference number. When configured using our analysis macros, the Object Results table on the right automatically lists all the traced branch tips, their lengths, their assigned branch reference numbers and in which window (i.e. time points 1–5) the branch appears. This information can be accessed using a macro language or exported for further analysis to a text file.

found it simplest to treat each branch as an individual entity rather than as a node in a tree structure. The cell tracing process is made faster since the operator tracing the cell needs only to connect segments physically without specifying which voxel along a segment should be counted as the branch point. The shortcoming of this approach is that branch-order information, if needed, must be extracted by a *post hoc* calculation of branching sites based on the locations of physical contacts.

Ultimately, we hope to implement automatic drawing routines that trace neuronal process branches in three dimensions without extensive user intervention. The main difficulty is that ambiguities in the original images are usually incorrectly drawn by such programs. Manual verification and editing steps then end up consuming as much time as would manual drawing from scratch. However, because such ambiguities are greatly reduced by two-photon imaging and by image processing with 3D deconvolution, it is likely that the application of algorithms for automated neuron tracing [39] will be feasible with our latest datasets. In combination with the user-friendly 3D drawing editor in Object-Image, automatic tracing would accelerate the analysis procedure tremendously.

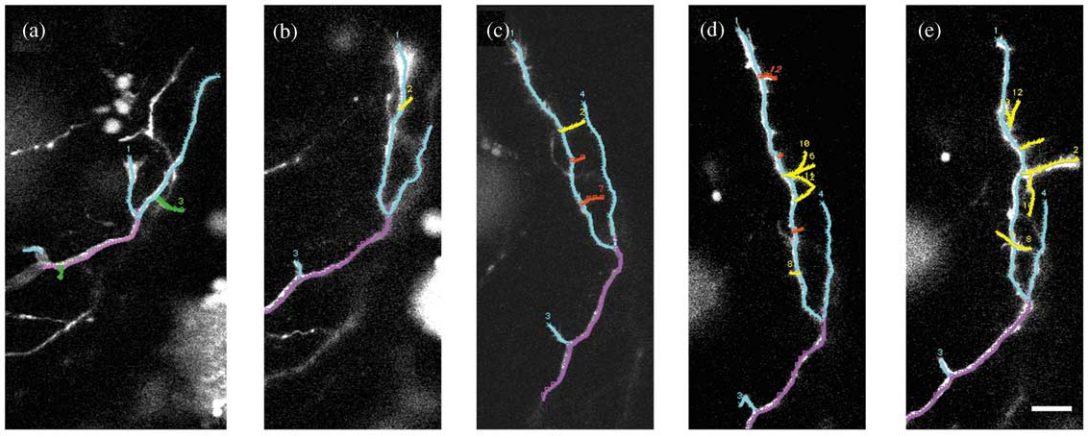


**Figure 7.** Automated display of branch dynamics properties. A custom morphological dynamics display macro color-codes each branch tip to reflect its dynamic growth behavior for time-lapse imaging. In this case, *green* branch tips are lost during the imaging period, *yellow* branch tips are added and maintained, *red* branch tips are transiently added and then lost, *light blue* indicates branch tips that are present for the entire imaging session, and *magenta* marks non-terminal branch structures. These axons were imaged every 2 h over an 8 h period, starting with a and ending with e. Scale bar = 10 μm.

*Branch dynamics analysis*. The axons and dendrites of developing neurons are highly dynamic structures that rapidly add and retract branch tips in an exploratory manner, reflecting the interactions with their environment as they grow. For analysis of the dynamic rearrangements of branch tips over time, we take advantage of the feature of Object–Image that permits additional information to be recorded together with the branch segment locations. The full set of *z*-series stacks for each of the multiple time points can be displayed simultaneously, or toggled between, for comparison while tracing their morphologies. After an individual branch is traced, our macro prompts the user for a branch reference number that will be recorded by the program along with information about the time point at which that branch was observed. If the same branch is present at multiple time points, that same reference number is applied to each occurrence. Thus when the drawings of the cell at each of the observation time points are completed, the program also will have compiled a comprehensive list of branches, their lengths, where they are located, and at what times they were observed. This information can be exported as a text file into spreadsheet software for more detailed analysis, such as average branch lifetimes.

This analysis can also be used to identify local hotspots of rapid branch additions and retractions or exceptionally stable sites within a complex arbor structure. Taking advantage of the branch reference number list compiled during the drawing step, we have created a display macro that draws each of the branches of a dendritic or axonal arbor in different colors based on whether the branch is stable, added, lost, or transient (i.e. both added and lost) over the observation period (Figure 7). The algorithm simply tests for all branch reference numbers, at what time points in the time-lapse series was a branch with this reference number present. It then assigns the branch to a "dynamics" category based on the results. This kind of visual demonstration of the dynamic additions and retractions of the branches in a neuronal arbor can offer important insights about cell growth and morphological development that a purely quantitative analysis might miss. For neurons with dendritic spines such as cortical pyramidal cells, a similar approach could be used for the study of spine dynamics [40,41].

*Sholl analysis*. Sholl analysis is a common method for characterizing the morphological complexity in the dendritic arbors of neurons [42]. The basic method is to draw a series of concentric circles of increasing radius, each centered at the soma of a traced cell, and then to count the number of intersections that occur between each of these circles and the dendritic branches in the drawing. Two-dimensional (2D) Sholl analysis can give misleading results when applied without meticulous correction for orientation to cells that lack radial symmetry. This problem can be avoided by performing Sholl analysis in three dimensions by counting intersec-

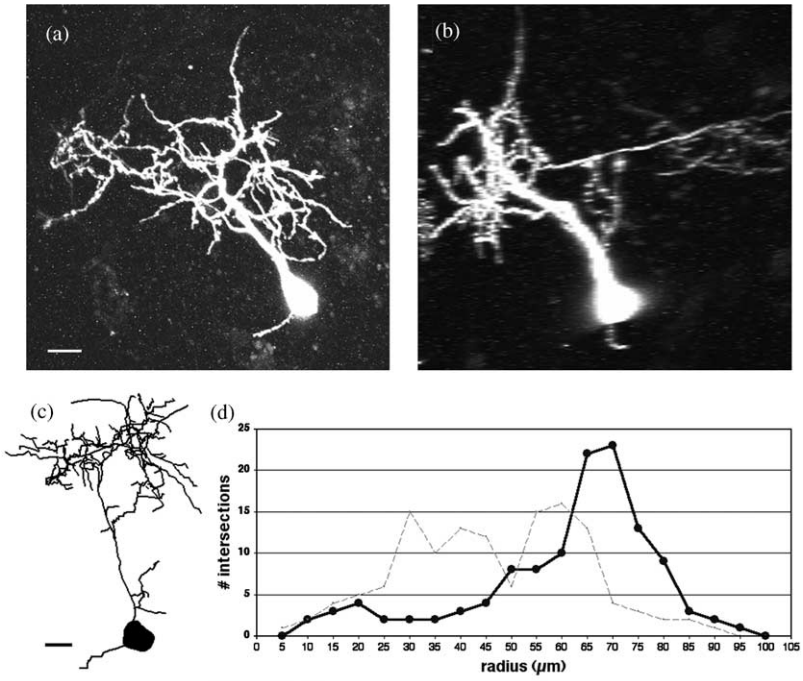


**Figure 8.** 3D Sholl analysis of dendrites. The dendritic tree of a GFP-expressing cell was traced as described in the text. (a) *x–y* projection of the two-photon *z*-series of the cell collapsed in the *z*-axis. (b) *z–y* projection of the same cell collapsed along the *x*-axis. (c) The 3D tracing of the dendritic arbor of this cell has been slightly rotated here to reveal the long axis of the primary dendrite. Note that the axon of this cell, which can be seen extending off to the left in A and to the right in B, is not included in this dendritic reconstruction. (d) 3D Sholl analysis macro was applied to the tracing data to count dendritic branch intersections with concentric Sholl spheres at 5 m radius steps from the cell body center (bold line). The effects of orientation on 2D Sholl analysis can introduce severe artifact. The dashed line shows the misleading result of a 2D Sholl analysis applied to the projected image of the cell as it appears in A, which fails to reveal the tufted shape of the neuron. Scale bar = 10 μm.

tions between the branches of a dendritic arbor and a series of concentric spherical shells. For Object–Image drawings, we have created a fast 3D Sholl analysis macro that simply tests for each segment in a drawing whether its endpoints are on opposite sides of a set of virtual Sholl spheres and then tabulates the results (Figure 8). Naturally, a conventional 2D Sholl analysis can also be performed using this method by first compressing the 3D neuron tracing into two dimensions.

The simple macros described above illustrate the versatility of neuron reconstruction using Object–Image. For our time-lapse analysis of neuronal branch dynamics, we created crude but useful macros to record and analyze 3D structural and temporal information about branches, some of which could not even have been performed with many existing professional software packages. Using Object–Image, other users, even those with only the most rudimentary programming experience, should be able to create macros tailored to their specific morphometry requirements.

## Conclusions

We have described recent advances in the collection and analysis of time-lapse, 3D morphology data. Two-photon laser scanning microscopy provides a marked improvement in tissue penetration and in both axial and temporal resolutions over confocal laser scanning microscopy with relatively few drawbacks. The majority of popular neuronal tracers for fluorescence microscopy that we examined also could be used for imaging by two-photon microscopy, using wavelengths of excitation light that are within the normal operating range of commercially available Ti: sapphire lasers. The observation that the two-photon excitation peaks of some dyes, such as Alexa594, are not simply derivative of their one-photon spectra predicts

the creation of a second generation of fluorescent dyes that will be selected for specific two-photon properties, such as suitability for double-labeling experiments.

For morphological analysis of 3D time-lapse data, there are two main prerequisites for any analysis software. First, the 3D coordinates of the points that make up the neuronal branches must be recorded and accessible for analysis. Second, it must be possible to apply a label to each individual branch in order to compare it at different time points. Most morphological reconstruction programs can satisfy the first demand, but surprisingly few provide for the second requirement. Object–Image, with the aid of some simple macro commands, can offer both.

## Acknowledgements

This work was supported by NIH awards to H.C. and to E.R. We thank Karel Svoboda, Peter O'Brien and Barry Burbach for guidance in constructing the two-photon microscope, Kendall Jensen and Kurt Haas for contributing labeled cells, Askhan Javaherian for generating the VAMP-GFP plasmid and the members of the Cline Lab for comments on the manuscript.

## References

1. Cline, H.T. (2001) *Current Opinions in Neurobiology* **11**: 118–126.
2. Cline, H.T., Edwards, J.A., Rajan, I., Wu, G.Y. & Zou, D.J. (1999) In vivo imaging of CNS neuron development. In: Yuste, R., Lanni, F. & Konnerth, A. (eds), *Imaging Neurons: A Laboratory Manual*. Cold Spring Harbor, NY: Cold Spring Harbor Laboratory Press, pp. 13.1–13.2.
3. Haas, H., Sin, W.-C., Javaherian, A., Li, Z. & Cline, H.T. (2001) *Neuron* **29**: 1–9.
4. Majewska, A., Yiu, G. & Yuste, R. (2000) *Pflugers Archives* **441**: 398–408.
5. Harris, W.A., Holt, C.E. & Bonhoeffer, F. (1987) *Development* **101**: 123–33.
6. Fine, A., Amos, W.B., Durbin, R.M. & McNaughton, P.A. (1988) *Trends in Neuroscience* **11**: 346–351.
7. O'Rourke, N.A., Cline, H.T. & Fraser, S.E. (1994) *Neuron* **12**: 921–934.
8. Cheong, W.F., Prahl, S.A. & Welch, A.J. (1990) *IEEE Journal of Quantum Electronics* **26**: 2166–2185.
9. Denk, W., Strickler, J.H. & Webb, W.W. (1990) *Science* **248**: 73–76.
10. Williams, R.M., Piston, D.W. & Webb, W.W. (1994) *Faseb Journal* **8**: 804–813.
11. Centonze, V.E. & White, J.G. (1998) *Biophysical Journal* **75**: 2015–2024.
12. Potter, S. M., Wang, C. M., Garrity, P. A. & Fraser, S. E. (1996) *Gene* **173**: 25–31.
13. Denk, W., Delaney, K.R., Gelperin, A., Kleinfeld, D., Strowbridge B. W., Tank, D.W. & Yuste, R. (1994) *Journal of Neuroscience Methods* **54**: 151–162.
14. Koester, H.J., Baur, D., Uhl, R. & Hell, S.W. (1999) *Biophysical Journal* **77**: 2226–2236.
15. Denk, W. & Svoboda, K. (1997) *Neuron* **18**: 351–357.
16. Xu, C., Williams, R.M., Zipfel, W. & Webb, W.W. (1996) *Bioimaging* **4**: 198–207.
17. Albota, M., Beljonne, D., Bredas, J.L., Ehrlich, J.E., Fu, J.Y., Heikal, A.A., Hess, S.E., Kogej, T., Levin, M.D., Marder, S.R., McCord-Maughon, D., Perry, J.W., Rockel, H., Rumi, M., Subramaniam, G., Webb, W.W., Wu, X.L. & Xu, C. (1998) *Science* **281**: 1653–1656.
18. Honig, H. & Hume, R.I. (1986) *Journal of Cell Biology* **103**: 171–187.
19. Kaethner, R.J. & Stuermer, C.A. (1992) *Journal of Neuroscience* **12**: 3257–3271.
20. Kuba, K. & Nakayama, S. (1998) *Neuroscience Research* **32**: 281–294.
21. Schmued, L., Kyriakidis, K. & Heimer, L. (1990) *Brain Research* **526**: 127–134.
22. Tsien, R.Y. (1998) *Annual Review of Biochemistry* **67**: 509–544.
23. Okada, A., Lansford, R., Weimann, J.M., Fraser, S.E. & McConnell, S.K. (1999) *Experiments in Neurology* **156**: 394–406.
24. Ruchhoeft, M.L., Ohnuma, S.-i., McNeil, L., Holt, C.E. & Harris, W.A. (1999) *Journal of Neuroscience* **19**: 8454–1863.
25. Horch, H.W., Kruttgen, A., Portbury, S.D. & Katz, L.C. (1999) *Neuron* **23**: 353–364.
26. Amsterdam, A., Lin, S. & Hopkins, N. (1995) *Development Biology* **171**: 123–129.
27. Fradkov, A.F., Chen, Y., Ding, L., Barsova, E.V., Matz, M.V. & Lukyanov, S.A. (2000) *FEBS Letters* **479**: 127–130.
28. Nonet, M.L. (1999) *Journal of Neurosci Methods* **89**: 33–40.
29. Shi, S.H., Hayashi, Y., Petralia, R.S., Zaman, S.H., Wenthold, R.J., Svoboda, K. & Malinow, R. (1999) *Science* **284**: 1811–1816.
30. Tsien, R.Y. (2000) Physiological indicators based on fluorescence resonance energy transfer. In: Yuste, R., Lanni, F. & Konnerth, A. (eds), *Imaging Neurons: A Laboratory Manual*. Cold Spring Harbor, NY: CSHL Press, pp. 55.1–55.10.
31. Wann, D.F., Woolsey, T.A., Dierker, M.L. & Cowan, W.M. (1973) *IEEE Transactions of Biomedical Engineering* **20**: 233–247.
32. Glaser, E.M., Tagamets, M., McMullen, N.T. & Van der Loos, H. (1983) *Journal of Neuroscience Methods* **8**: 17–32.
33. Ratto, G.M. & Usai, C. (1991) *Journal of Neuroscience Methods* **36**: 33–43.
34. Stockley, E.W., Cole, H.M., Brown, A.D. & Wheal, H.V. (1993) *Journal of Neuroscience Methods* **47**: 39–51.
35. Vischer, N.O., Huls, P.G., Ghauharali, R.I., Brakenhoff, G.J., Nanninga, N. & Woldringh, C.L. (1999) *Journal of Microscopy* **196 (Part 1)**: 61–68.

36. Haas, H., Shi, S.H., Malinow, R. & Cline, H.T. (2001) *Society of Neuroscience Abstracts*, Vol. 27, Program No. 902.8.
37. Ruthazer, E.S. & Cline, H.T. (2001) *Society for Neuroscience Abstracts*, Vol. 27, Program No. 363.19.
38. Sin, W.-C., Li, Z. & Cline, H.T. (2001) *Society for Neuroscience Abstracts*, Vol. 27, Program No. 7.2.
39. Cohen, A.R., Roysam, B. & Turner, J.N. (1994) *Journal of Microscopy* **173 (Part 2)**: 103–114.
40. Dailey, M.E. & Smith, S.J. (1996) *Journal of Neuroscience* **16**: 2983–2994.
41. Lendvai, B., Stern, E.A., Chen, B. & Svoboda, K. (2000) *Nature* **404**: 876–881.
42. Sholl, D.A. (1953) *Journal of Anatomy (London)* **87**: 387–406.